Localized water mist method enabling superior premixed hydrogen-methane-air deflagration mitigation in semi-confined space

Yuanchen Xia [a, 1] Jinnan Zhang [a, 1], Bin Zhang [a, *], Boqiao Wang [a], Li Chen [a], Ruiqi Wang [a], Jihao Shi [b], Wanqing Wu [a], Kayvan Pazouki [c]

[a] Marine Engineering College, Dalian Maritime University, Dalian 116026, Liaoning, China

[b] Department of Building Environment and Energy Engineering, The Hong Kong Polytechnic University, Kowloon, Hong Kong, China

[c] School of Engineering, Newcastle University, Newcastle upon Tyne, UK

[1] These authors contributed equally to this work and should be considered co-first authors.

* Corresponding author

E-mail address: zb_2010@dlum.edu.cn (B. Zhang)

Abstract

To effectively mitigate hydrogen-methane-air deflagrations in semi-confined space, we propose a Localized Water Mist(LWM) method. The results demonstrate that when the 8-μm LWM is sprayed near the igniter, the flame velocity and overpressure decrease by 38.8% and 30.1%, respectively. However, the 45-μm LWM exhibits enhanced effect. When the 45-μm LWM is sprayed near the obstacle, it shows superior deflagration mitigation capabilities. Reciprocally, the 8-μm LWM has few mitigation effect. Subsequently, the deflagration mitigation mechanism of LWM is analyzed. The small-diameter LWM has large surface area, sufficient interaction with the flame surface and minimal turbulence interference near the igniter. In contrast, large-diameter LWM is broken into small-size particles by the shock wave near the obstacle, which are able to enter vortex flames absorbing heat quickly. Additionally, vaporized WM mitigates deflagration by reducing the generation rate of the main radicals(OH, H, and O) through reactions R1, R3, R50, R86, R119, and R120.

Keywords

Localized water mist; Hydrogen-methane-air deflagrations; Flame instability; Cellular flame; Mitigation mechanism

1 Introduction

Methane currently is a common fuel in the process industry and as a result, this has contributed to massive greenhouse gas emissions by this industry [1, 2]. As environmental protection and low carbon become the main concern of process industrial production, hydrogen as an alternative source of energy has gained popularity [3-6]. However, the storage and transportation costs of hydrogen energy are extremely high, which puts a hold on the large-scale application of hydrogen energy in this industry [7-9]. As an alternative, direct injection of hydrogen into the natural gas pipeline network for transportation and storage is a good option, which not only decreases carbon emissions but also does not require additional storage and transportation costs [10-12]. Mixing hydrogen with methane can not only increase the laminar combustion velocity of methane but also broaden the combustion limit and improve the reactivity of the fuel [13-15]. Meanwhile, the high diffusivity of hydrogen and the phenomenon of hydrogen embrittlement increase the risk of hydrogen-methane mixture leakage [16, 17]. Once a leakage and subsequent explosion accident occur, this will lead to serious economic losses [18, 19]. Hydrogen-methane mixtures are widely used and stored in various scenarios, which consequently increases the possibilities for leakage and explosion accidents [20-23]. Therefore, it is imperative and crucial to conduct dedicated research on deflagration mitigation specifically for these scenarios.

Up to now, widely used deflagration suppressants in the process industry include dry powder, inert gas, fluorocarbon, and water mist (WM) [24-27]. Five different types of dry powders (calcium carbonate, aluminum powder, silicon dioxide, ABC powder, and BC powder) were applied to mitigate hydrogen-air deflagrations within a confined space [28, 29]. Among them, silicon dioxide dry powder exhibited the most effective mitigation of hydrogen-air deflagrations, followed by calcium carbonate, ABC powder,

BC powder, and aluminum powder [30]. Furthermore, smaller particle size of dry powders showed better mitigation effects [31]. In contrast to solid particles of dry powders, inert gases have more extensive contact with the flame surface, leading to more satisfactory deflagration mitigation results. Research on hydrogen-air deflagrations in inert gas atmosphere within a confined space revealed that, in terms of mitigating deflagration overpressure, CO_2 performed best, followed by He, Ar, and N_2. Further investigation of CO_2 indicated that its mitigation of hydrogen-air deflagrations is achieved by mitigating laminar burning velocity, which is attributed to the reduction in thermal diffusivity, flame temperature, and active radicals [32]. Fluorocarbons achieve even better deflagration mitigation than CO_2 at lower volume concentrations [33]. Studies on the deflagration mitigation mechanism of fluorocarbon showed that it primarily inhibit the instability of hydrogen-air flame, thereby reducing the extent of hydrogen-air flame acceleration and mitigating deflagrations [26]. However, all of these suppressants have certain usage limitations, as their toxicity and potential for causing suffocation may pose secondary hazards. In contrast, WM not only poses no harm to humans but also possesses the advantages of the aforementioned suppressants, making it highly favored by researchers.

Experimental studies within confined space indicated that WM parameters significantly influence the effectiveness of deflagration mitigation, with WM having an average size of 6-50 μm being able to significantly reduce deflagration overpressure and flame velocity [34-36]. In-depth research demonstrated that WM achieves a notable reduction in flame velocity and deflagration overpressure through processes such as evaporative cooling, oxygen dilution, heat radiation shielding, and chain reaction inhibition [37-41]. Although the deflagration mitigation effect of small-diameter WM is substantial, literature data [35] indicates a significant reduction in the deflagration

4

mitigation effectiveness of small-diameter WM under obstacle conditions. Despite the significant mitigation effect of 6-50 μm WM under spraying throughout the entire deflagration space conditions, researchers were unexpected to find a promoting effect when using 45 μm WM in localized region, while larger droplets of 160 μm demonstrated excellent mitigation effect [42]. However, quantitative studies based on CFD indicated that this phenomenon is related to the breaking effect of the deflagration shockwave on droplets [43]. WM with a diameter larger than 150 μm was broken into smaller droplets. And for droplets smaller than 10 μm, they were dispersed by the shockwave, leading to the loss of deflagration mitigation effect [37, 44]. All these signs indicate the crucial importance of spray position selecting for the deflagration mitigation effect of WM with different diameters. On the other hand, using large-size water mist introduces external disturbances to the premixed flame. Studies have indicated that under external disturbances like shock waves and particles, deflagration flames might transform into detonation [45, 46]. In strong flame acceleration state, precursor shock waves focus continuously due to reflections on the walls, concentrating energy locally and eventually triggering detonation [47, 48]. However, the acceleration effect of water mist particles mainly manifests as the wrinkling of the flame surface induced by these particles, leading to an increase in flame surface area and thus accelerating the flame [49]. Additionally, in the preheating region, water mist particles that do not evaporate completely in time create a series of small obstacles [50]. As the flame passes through the gaps between these obstacles, it gets entrained and curled in the wake flow, interacting with turbulence, causing flame fragmentation, which further promotes the acceleration of the flame [51]. With the continuous accumulation of compression waves, the flame accelerates continuously and transforms into detonation when the reaction front overlaps with the compression waves. Once the flame

accelerates to the detonation state, the mitigation mechanism of water mist shifts to absorbing the momentum of shock waves leading to the decoupling of the detonation wave from the combustion wave [52, 53]. This requires very high water mist loading ratios [54]. Therefore, selecting appropriate spray locations and diameters is crucial for the water mist to exert its mitigation effect, preventing flame acceleration. However, as of now, research in this area is still lacking.

The majority of published papers have focused on studying WM mitigation of deflagrations within confined space. Additionally, WM is typically sprayed throughout the entire deflagration space. However, this spraying method and deflagration scenario may not accurately represent the real engineering situations of using LWM for deflagration mitigation. To date, there is a lack of research data on the use of spray methods and the mitigation of hydrogen-methane-air deflagrations in semi-confined space. Therefore, this work aims to investigate a localized water mist (LWM) method to achieve excellent mitigation of hydrogen-methane-air deflagrations in semi-confined space and explore the mitigation mechanism of this method. The mechanism includes exploring the effects of spray location and WM diameter on the effectiveness of deflagration mitigation. The research findings will provide theoretical references for the prevention and control of hydrogen-methane-air deflagration disasters in the process industry.

2 Experimental device and method

In this work a series of experimental equipment were used, which are shown in Fig. 1. It mainly includes high-speed camera, semi-confined deflagration tube, gas distribution system, data collection instrument and WM generating instrument. Detailed parameters of the experimental equipment can be found in Supplementary Material. All

experiments were completed under the same environmental circumstance, the ambient temperature is 298 K ± 2 K and the ambient humidity is 35% ± 5%. So as to assure the accuracy and repeatability of the experimental results, all the experiment case was iterative for 3 to 6 times under similar working condition. In this work, the error of the peak flame speed and peak deflagration overpressure value for each repeated experiment is no more than 5%.

The WM generation system includes ultrasonic WM generation system and two-fluid WM generation system. So as to preclude the impact of ions on the experimental results, distilled water was used. The 8 μm WM is generate by ultrasonic WM generating instrument, and the 15, 30, 45 μm WM are generated by two-fluid WM generating instrument. Table 1 lists the detailed parameters of the WM used in this work. The size and the concentration of the WM defined as:

$$\bar{d}_{32} = \frac{\sum nd^3}{\sum nd^2} \tag{1}$$

$$\omega = \frac{W_f \cdot t}{V} \tag{2}$$

The measurement of the average diameter of water mist is based on the laser particle sizer, and the detailed particle size differential distribution can be found in Supplementary Material. For this research, the working principle of the gas distribution system can be found in the literature [55]. The ER and HBR are defined as [56, 57]:

$$\Phi = \frac{n_{fuel}/n_{Air}}{\left(n_{fuel}/n_{Air}\right)_{st}} \tag{3}$$

$$X_{H_2} = \frac{V_{H_2}}{V_{H_2} + V_{CH_4}} \tag{4}$$

The calculation method of flame propagation velocity is defined as:

$$\frac{f}{l} = \frac{f_{t_i} - f_{t_{i+1}}}{S_{t_i} - S_{t_{i+1}}} \tag{5}$$

$$v = \frac{S_{t_i} - S_{t_{i+1}}}{t_i - t_{i+1}} \tag{6}$$

In our work, the deflagration tube is designed into four parts, of which three LWM release positions are designed as P1, P2 and P3. P1, P2 and P3 are described in detail in Supplementary Material. The internal dimensions of the deflagration chamber are 0.82 m × 0.16 m × 0.16 m. The external dimensions of the obstacle size of the obstacle are 0.03 m × 0.16 m × 0.08 m. The obstacle distance from ignition source is 0.31 m. The details of experimental procedures and operations can also be found in Supplementary Material.

3 Results and discussion

3.1 Impact of localized WM on deflagration characteristic in unobstructed semi-confined space

Four different average sizes were used in this work to explore the impact of WM average size on flame morphology. Fig. 2 shows the flame morphology under the conditions of micron-level WM with different sizes. The cellular structure appeared on the flame surface under the 8 μm, 15 μm, 30 μm, and 45 μm WM. For more detailed cellular structure pictures, please refer to the Supplementary Material. This indicates that micron-level WM enhances the destabilization of the flame surface [58, 59]. The size of the cellular structure decreased with the decrease in the average size of the WM [60]. The 8 μm WM allows the flame surface to maintain its finger morphology and propagate forward. However, the 15 μm, 30 μm, and 45 μm WM changed the flame structure and localized extinguishment occurred. This may be related to the effect that

WM can block thermal radiation [61]. The 8 μm WM, having a large surface area, quickly evaporates in front of the flame without penetrating the flame surface, resulting in the appearance of a cellular structure on the flame surface. As the average size of micron-level WM increases to 15 μm, 30 μm, and 45 μm, the surface area and evaporation rate decrease. The WM particles that cannot evaporate completely enter the flame surface, leading to a decrease in local flame temperature and localized extinguishment [35]. This further alters the finger-shaped structure of the flame, causing the flame surface to become more distorted.

To enhance the credibility of the research findings, the physical deflagration mitigation effect of WM is analyzed using premixed combustible gas with Φ=1.0, which represents the highest deflagration intensity. Fig. 3 (a-c) illustrates the influence of micron-level WM on the deflagration characteristics of hydrogen-methane-air mixtures with various HBR. For the case of HBR=10% without WM spraying, the use of 8 μm WM exhibits the greatest mitigation in flame propagation velocity and peak overpressure reduction. Specifically, the PFPV is reduced by 38.8%, and the PDOP is reduced by 30.1%. As the WM diameter increases, the mitigation effect gradually weakens. However, when the WM diameter reaches 45 μm, it shows a promoting effect. The same trend is observed with increasing HBR, although the mitigation effect of the WM diminishes and its promoting effect strengthens. The smaller average size of 8 μm WM leads to minimal perturbation on the flame surface, faster evaporation, and better mitigation effect. On the other hand, the larger average size of 45 μm WM results in slower evaporation. This WM, which does not undergo rapid evaporation, tends to destabilize the flame structure, leading to a more pronounced promoting effect.

The mitigation impact of micron-level WM with the same average size gradually weakens as the HBR increases. Conversely, the enhancement impact of 45 μm WM

increases steadily. This is because as the HBR increases, the flame temperature also rises, while the heat absorbed by 8 μm, 15 μm, and 30 μm WM remains constant, resulting in a reduced mitigation impact. Moreover, as the HBR increases in the mixture, the flame instability also intensifies, and the presence of 45 μm WM itself acts as obstacles, further enhancing flame instability and consequently promoting deflagration.

The action process of WM with different diameters in the flame surface can be divided into two processes: heat absorption and evaporation. The lifetime of WM particles on the flame surface is determined by the time it takes for the particles to rise from room temperature to 100 ℃ and undergo liquid vaporization at 100 ℃ to become steam at 100 ℃ [36]:

$$t_h = \frac{c_w \rho_w d_0}{6h} \ln \frac{T_f - T_0}{T_f - T_s} = \frac{c_w \rho_w d_0^2}{6\lambda Nu} \ln \frac{T_f - T_0}{T_f - T_s} \tag{7}$$

$$t_{evp} = \frac{c_p \rho_w d_0^2}{8\lambda \ln \left[1 + \frac{\lambda_0}{\lambda} \frac{c_p}{L} (T_f - T_s) \right]} \tag{8}$$

$$t_l = t_h + t_{evp} \tag{9}$$

The calculation results of Eqs. (7-9) are presented in Fig. 4. According to the results, the heating time, evaporation time, and lifetime are greatly influenced by the particle size. For 8 μm water mist, the heating and evaporation process takes 0.3 ms. For 15 μm, 30 μm, and 45 μm WM, the process takes 1.2 ms, 4.9 ms, and 11 ms respectively. The lifetime of 45 μm WM is 36.7 times that of 8μm WM, inevitably leading to a sharp decrease in its mitigation effectiveness.

During laminar the premixed deflagration process, the flame surface is very thin and this surface can be divided into three parts: the preheating region, reaction region, and burned region. Fig. 5 illustrates the involvement of micron-level WM with different average sizes in the deflagration process. Larger average-sized WM particles struggle

to evaporate quickly on the flame surface and fail to exert the desired deflagration mitigation impact. Instead, they act as obstacles, inducing turbulence in the deflagration area, ultimately intensifying the consequences of deflagration. This turbulence can cause wrinkling and severe deformation of the flame surface (Fig. 2). On the contrary, smaller average-sized WM particles evaporate more quickly, allowing them to rapidly absorb heat from the combustion region and reduce flame temperature, thereby achieving excellent deflagration mitigation. The vaporization of WM produces a large number of water molecules, which participate in the chemical combustion process, weakening the chain reactions and further mitigating the deflagration. The chemical mitigation effect of fine WM is mainly attributed to the attenuation of the main active free radicals [40]. Vaporized WM mitigates deflagration by reducing the generation rate of the main radicals(OH, H, and O) through reactions R1, R3, R50, R86, R119, and R120. Table 2 shows the correspondence between elementary reactions involving water molecules and their steps number. The more detailed analysis on the physical and chemical mitigation mechanisms of vaporized WM can be referred to in the Supplementary Material.

3.2 Impact of obstacle on deflagration characteristic in semi-confined space

Fig. 6 shows the dynamic evolution of the flame surface under both without obstacle and obstacle conditions. Under the no obstacle condition, when t∈(0, 22 ms), the flame surface propagates with a semi-spherical shape and remains smooth throughout the propagation process. When t ≥ 22 ms, the flame surface begins to exhibit finger shape propagation due to the constraint of the container wall, until it reaches the opening of the tube (t = 69 ms). Throughout this process, the flame surface can be

considered to be in a laminar deflagration state. Under the obstacle condition, the dynamic evolution of the flame surface can be divided into four stages: (1) The semi-spherical flame stage t∈ (0, 22 ms), where the flame propagation is primarily controlled by chemical deflagration processes, and heat, momentum, and energy exchange occur between the deflagration products and unburned gas molecules on both sides of the flame surface. (2) The finger shape flame stage t∈ (22, 32 ms), where the flame propagation is constrained by the wall, resulting in a transition to a finger shape. (3) The jet flame stage t∈ (32, 45 ms), where the presence of obstacle leads to a reduction in the cross-sectional area as the flame crosses the obstacles, converting the pressure energy of the burned gas into velocity energy, significantly increasing the flame speed, and forming a jet flame. (4) The vortex flame stage t∈ (45, 48 ms), where after crossing the obstacle, the flame experiences boundary layer separation effects and shear flow, rapidly transitional into a turbulent vortex flame. Within the turbulent vortex, the deflagration of the flame exhibits characteristics of volume deflagration rather than surface propagation.

Fig. 7 displays the occurrence of flame reverse propagation in the left front of the obstacle for ER values of 0.8, 1.0, and 1.2, with the degree of flame front wrinkling increasing as HBR increases. Notably, when ER is 0.8, back propagation of the flame appears in the upper left corner of the obstacle. Furthermore, the back propagation flame in the upper left corner of the obstacle becomes stronger and more prominent with increasing HBR at ER = 0.8. However, as the mixture ER increases, the back propagation flame in the upper left corner of the obstacle gradually disappears. This phenomenon is attributed to the enhanced stability of the mixed gas resulting from an increased effective Lewis number. In summary, obstacle leads to the formation of jet flame and vortex flame, significantly enhancing the intensity of the deflagration. Due

to the inherent instability of hydrogen, vortex flame is observed not only on the left side of the obstacle but also in the upper left corner, in addition to the vortex flame on the left side of the obstacle.

A series of experiments were conducted to investigate the impact of obstacle on the flame propagation velocity (PFV) and overpressure in hydrogen-methane-air deflagration. Fig. 8 (a) illustrates the flame velocity and overpressure without obstacles, while Fig. 8 (b) presents the flame velocity and overpressure with obstacle. For a specific ER, the PFV increases as the HBR increases. Similarly, for a specific HBR, the PFV initially increases and then decreases as the ER increases. The addition of obstacles in the experimental tube leads to a significant increase in both peak flame velocity and peak overpressure. To assess the extent of the influence of obstacles on flame velocity and deflagration overpressure, the peak flame velocity rise ratio (R_v) and the peak overpressure rise ratio (R_P) are defined:

$$R_v = \frac{v_{obstacle} - v}{v} \tag{10}$$

$$R_p = \frac{P_{obstacle} - P}{P} \tag{11}$$

Fig. 9 shows the R_v and R_P with different ER and HBR. For different ER and HBR, $1.17 \leq R_v \leq 1.9$, $0.7 \leq R_P \leq 1.92$. This shows that obstacle caused the astonishing amount of increase in peak flame velocity and peak overpressure at different ER and HBR. The strong promotion impact of obstacle on deflagration will pose a great challenge to the deflagration mitigation impact of micron-level WM.

3.3 Coupled impact of localized water mist and obstacle on deflagration characteristic in semi-confined space

Fig. 10 illustrates the combined effect of 45 μm WM and obstacle on the flame structure under ER=1.0 and HBR=10% condition. Based on Fig. 7 (b), it can be observed that in the absence of WM and with obstacle, vortex flames are not present in the upper-left corner of the obstacle, but larger vortex flames occur only on the left side of the obstacle. However, upon observing Fig. 10, it is evident that after spraying WM, vortex flames appear in the upper-left corner of the obstacle, and the large vortex flames on the left side of the obstacle become more wrinkled and distorted. This further indicates that WM promotes flame instability and propagation. When the spray position is changed, the degree of flame surface instability also varies. At spray position P1, which is closest to the ignition source, the flame surface exhibits the highest degree of wrinkling and distortion. At spray position P2, which is closest to the obstacles, the degree of flame surface wrinkling and distortion is slightly lower. At spray position P3, which is farthest from the ignition source, the degree of flame surface wrinkling and distortion is the same as that in the absence of WM. This shows that the spray will cause serious instability in flame propagation process, and the closer the spray position is to the ignition source, the greater the level of flame instability. So the spray position has a great influence on the inhibitory effect of water mist.

As shown in Fig. 11 (a) and (b), the lowest flame propagation velocity (FPV) and peak deflagration overpressure (PDOP) are observed when 8 μm and 15 μm WM are released at P1, indicating the best mitigation impact. The mitigation impact of 8 μm WM is superior to that of 15 μm WM due to its smaller average size, resulting in a faster evaporation rate. Additionally, the presence of the obstacle allows more interaction time between the 8 μm WM and the flame surface, enhancing both chemical

and physical mitigation in the local P1 area. Moving on to Fig. 11 (c) and (d), when 30 μm and 45 μm WM are released at P2, the FPV and PDOP are the lowest, demonstrating the best mitigation impact. Moreover, the mitigation impact of 45 μm WM surpasses that of 30 μm WM. The mitigation impact of micron-level WM is closely tied to its average size. The mitigation impact at P2 consistently outperforms that at P3 due to the presence of the obstacle, resulting in a higher density of micron-level WM at P2 and a shorter interaction time between micron-level WM and the flame at P3. As the average size of micron-level WM increases at P1, the mitigation impact gradually weakens until a deflagration-promoting impact occurs. Micron-level WM released at different positions exhibits varying mitigation impacts, highlighting the positional influence. Micron-level WM particles of 8 μm, 15 μm, and 30 μm released near the igniter demonstrate mitigation impact, while the release of 45 μm WM exhibits an enhancing impact. The 45 μm WM significantly affects the flame structure and induces turbulence, especially in the initial stage of flame development due to the presence of WM, acting as obstacles. The strong instability of the hydrogen-methane-air flame leads to the largest average size of 45 μm WM, causing substantial disturbance to the flame surface. Although the mitigation impact of micron-level WM itself is less prominent, the enhancement impact on flame surface disturbance ultimately takes precedence, resulting in an enhancing impact. Furthermore, the mitigation impact of released 45 μm WM at P2 surpasses that of 30 μm WM. The obstacle enhances flame propagation velocity and deflagration intensity. By decomposing 45 μm WM particles into smaller ones, the physical mitigation impact can be further enhanced [58]. Smaller micron-level WM particles are more susceptible to being washed away by high-speed airflow, leading to a greater decrease in micron-level WM concentration in the local area and a diminished physical and chemical mitigation impact.

Fig. 12 illustrates the interaction process between micron-level WM and the flame at three positions (P1, P2, and P3). Based on Fig. 6, obstacle leads to the formation of jet flame and vortex flames. Jet flame has the characteristics of high-speed propagation. Smaller micron-level WM particles are more easily dispersed by high-speed airflow [58]. So the smaller the diameter, the more water mist will be lost under the action of the shock wave of jet flame. The difference between vortex flame and laminar deflagration is that the combustion reaction occurs in an extremely thin region during, that is, the flame spreads in the form of a surface. The characteristic of a vortex flame is that it exhibits volumetric combustion, that is, the combustion reaction occurs violently within the entire vortex. The 45 μm WM particles are broken into smaller water mist particles under the action of the shock wave of the jet flame [37]. These droplets breakup process is primarily determined by the Weber number [62]:

$$We = \frac{\rho_g u_g^2 d}{\sigma} \qquad (12)$$

The Weber number represents the ratio of inertial forces to surface tension forces experienced by water droplets in gas-liquid two-phase flow fields. A higher Weber number indicates greater inertial forces, making water droplets more prone to breakup. Literature research data indicates that the critical breakup Weber number for water droplets is $We_{break} = 10$ [63]. In our work, ρ_g=1.29kg/m^3, σ=54×10^{-3}N/m [64]. Based on Fig. 11, it can be observed that the peak flame velocity under no WM conditions can reach 80 m/s. Consequently, the critical breakup size at this velocity is 65.4 μm. The particle size distribution of the 45 μm water mist follows a normal distribution overall (refer to Supplementary Material). Particles larger than 65.4 μm constitute over 20% of the differential distribution. Therefore, these large WM particles can be broken apart into small particles by the high-speed gas flow. And then these small particles enter the

vortex flame under the action of the reverse flow field, continuously reducing the flame temperature, and participating in the physical and chemical suppression process. The occurrence of vortex flames is the result of the strong turbulence of the flow field caused by obstacles and the separation of the boundary layer. Therefore, the turbulence caused by small particles of water mist can be almost ignored compared with obstacles.

4 Conclusions

A localized water mist method is proposed to mitigate efficiently hydrogen-methane-air deflagrations in semi-confined space. A series of experiments and numerical studies were conducted to investigate the deflagration mitigation effects of localized water mist and the associated physical and chemical deflagration inhibition mechanisms. The following conclusions are obtained:

(1) Both water mist and the blending of hydrogen can enhance premixed flame instability. The water mist leads to the cellular structure of the hydrogen-methane-air flame surface. The blending of hydrogen in methane causes a vortex flame to appear in the upper left corner of the obstacle, and the vortex flame becomes larger as the hydrogen blending ratio increases, under lean burnning conditions.

(2) Under the no obstacle condition, 8-30 μm WM show the deflagration mitigation impact and 45 μm WM shows the deflagration enhanced impact. The large size WM which cannot evaporate quickly caused turbulence in the form of obstacles, which is the main reason for the deflagration enhanced impact.

(3) With the obstacle condition, when the 45 μm LWM is sprayed near the obstacle, it shows superior deflagration mitigation capabilities. Reciprocally, the 8-μm LWM has few mitigation effect. The smaller droplets are dispersed by the shockwave of the jet flame, whereas the larger 45 μm WM break into smaller WM under the

influence of the shockwave, exhibiting excellent deflagration mitigation effect.

(4) Water mist particles achieve physical cooling of the flame through heat absorption and evaporation processes. Vaporized WM mitigates deflagration by reducing the generation rate of the main radicals(OH, H, and O) through reactions R1, R3, R50, R86, R119, and R120 (decay chain reaction).

(5) The effects of LWM on deflagration flame can be divided into two types, mitigation and enhancement. The final effect depends on the sum of the above two effects. The appropriate choice of spray position and spray diameter is very crucial important for the mitigation impact of water mist performanced.

Based on the data reported in this work, two recommendations are made for the use of WM to mitigate hydrogen-methane-air deflagrations in industrial processes and prevent deflagration escalation: (1) Small diameter WM should be sprayed where potential ignition source may occur. (2) Large diameter WM should be sprayed in places with obstacles (equipment, pipeline).

Acknowledgments

References

[1] Chen W, Tang H, He L, Zhang Y, Ma W. Co-effect assessment on regional air quality: A perspective of policies and measures with greenhouse gas reduction potential. Sci Total Environ. 2022;851:158119.

[2] Dong K, Dong X, Jiang Q, Zhao J. Assessing energy resilience and its greenhouse effect: A global perspective. Energy Econ. 2021;104.

[3] Yue M, Lambert H, Pahon E, Roche R, Jemei S, Hissel D. Hydrogen energy systems: A critical review of technologies, applications, trends and challenges. Renew Sust Energ Rev. 2021;146.

[4] Rabiee A, Keane A, Soroudi A. Technical barriers for harnessing the green hydrogen: A power system perspective. Renew Energ. 2021;163:1580-7.

[5] Pingkuo L, Xue H. Comparative analysis on similarities and differences of hydrogen energy development in the World's top 4 largest economies: A novel framework. Int J Hydrog Energy. 2022;47:9485-503.

[6] Taipabu MI, Viswanathan K, Wu W, Hattu N, Atabani AE. A critical review of the hydrogen production from biomass-based feedstocks: Challenge, solution, and future prospect. Process Saf Environ Prot. 2022;164:384-407.

[7] Keçebaş A, Kayfeci M. Hydrogen properties.　Solar Hydrogen Production2019. p. 3-29.

[8] Liu Z, Xiong Y, Zhu Z, Zhang Z, Liu Y. Effects of hydrogen addition on combustion characteristics of a methane fueled MILD model combustor. Int J Hydrog Energy. 2022;47:16309-20.

[9] Taib NM, Mansor MRA, Wan Mahmood WMF. Combustion characteristics of hydrogen in a noble gas compression ignition engine. Energy Rep. 2021;7:200-18.

[10] Froeling HAJ, Dröge MT, Nane GF, Van Wijk AJM. Quantitative risk analysis of a hazardous jet fire event for hydrogen transport in natural gas transmission pipelines. Int J Hydrog Energy. 2021;46:10411-22.

[11] Witkowski A, Rusin A, Majkut M, Stolecka K. Analysis of compression and transport of the methane/hydrogen mixture in existing natural gas pipelines. Int J Press Vessel Pip. 2018;166:24-34.

[12] Messaoudani Zl, Rigas F, Binti Hamid MD, Che Hassan CR. Hazards, safety and knowledge gaps on hydrogen transmission via natural gas grid: A critical review. Int J Hydrog Energy. 2016;41:17511-25.

[13] Tang G, Jin P, Bao Y, Chai WS, Zhou L. Experimental investigation of premixed combustion limits

of hydrogen and methane additives in ammonia. Int J Hydrog Energy. 2021;46:20765-76.

[14] Klell M, Eichlseder H, Sartory M. Mixtures of hydrogen and methane in the internal combustion engine – Synergies, potential and regulations. Int J Hydrog Energy. 2012;37:11531-40.

[15] Zhao K, Cui D, Xu T, Zhou Q, Hui S, Hu H. Effects of hydrogen addition on methane combustion. Fuel Process Technol. 2008;89:1142-7.

[16] Okonkwo PC, Barhoumi EM, Ben Belgacem I, Mansir IB, Aliyu M, Emori W, et al. A focused review of the hydrogen storage tank embrittlement mechanism process. Int J Hydrog Energy. 2023.

[17] Yang F, Wang T, Deng X, Dang J, Huang Z, Hu S, et al. Review on hydrogen safety issues: Incident statistics, hydrogen diffusion, and detonation process. Int J Hydrog Energy. 2021;46:31467-88.

[18] Rui S, Wang C, Guo S, Jing R, Li Q. Hydrogen-air explosion with concentration gradients in a cubic enclosure. Process Saf Environ Prot. 2021;151:141-50.

[19] Zhang K, Du S, Chen H, Wang J, Zhang J, Guo Y, et al. Effect of hydrogen concentration on the vented explosion of hydrogen–air mixtures in a 5-m-long duct. Process Saf Environ Prot. 2022;162:978-86.

[20] Zhu J, Pan J, Zhang Y, Li Y, Li H, Feng H, et al. Leakage and diffusion behavior of a buried pipeline of hydrogen-blended natural gas. Int J Hydrog Energy. 2023;48:11592-610.

[21] Ekoto IW, Merilo EG, Dedrick DE, Groethe MA. Performance-based testing for hydrogen leakage into passenger vehicle compartments. Int J Hydrog Energy. 2011;36:10169-78.

[22] Takeno K, Okabayashi K, Kouchi A, Misaka N, Hashiguchi K. Concentration fluctuation and ignition characteristics during atmospheric diffusion of hydrogen spouted from high pressure storage. Int J Hydrog Energy. 2017;42:15426-34.

[23] Lacome JM, Jamois D, Perrette L, Proust CH. Large-scale hydrogen release in an isothermal confined area. Int J Hydrog Energy. 2011;36:2302-12.

[24] Zhang S, Wen X, Guo Z, Zhang S, Ji W. Experimental study on the multi-level suppression of N2 and CO2 on hydrogen-air explosion. Process Saf Environ Prot. 2023;169:970-81.

[25] Shang S, Bi M, Zhang Z, Li Y, Gao Z, Zhang C, et al. Synergistic effects of isobutene and carbon dioxide on suppressing hydrogen-air explosions. Int J Hydrog Energy. 2022;47:25433-42.

[26] Gao M, Bi M, Ye L, Li Y, Jiang H, Yang M, et al. Suppression of hydrogen-air explosions by hydrofluorocarbons. Process Saf Environ Prot. 2021;145:378-87.

[27] Ji H, Lu R, Yang K, Jiang J, Xing Z, Guo J. Experimental study on methane explosion suppression

by heptafluoropropane drived modified ABC powder. Process Saf Environ Prot. 2023;170:623-35.

[28] Chen J, Chen K, Shi W, Pan Z, Yang J, Zhang G, et al. The preparation of novel core–shell suppressor and its suppression mechanism on coal dust explosion flame. Fuel. 2022;313.

[29] Luo Z, Wang T, Tian Z, Cheng F, Deng J, Zhang Y. Experimental study on the suppression of gas explosion using the gas–solid suppressant of CO2/ABC powder. J Loss Prev Process Ind. 2014;30:17-23.

[30] Fan R, Jiang Y, Qiu R. A compound silica-trifluoroacetyl powder for fire suppressant: Preparation, characterization and suppression mechanism discussion. Fire Saf J. 2020;115.

[31] Chen Z, Fan B, Jiang X. Suppression effects of powder suppressants on the explosions of oxyhydrogen gas. J Loss Prev Process Ind. 2006;19:648-55.

[32] Li Y, Bi M, Huang L, Liu Q, Li B, Ma D, et al. Hydrogen cloud explosion evaluation under inert gas atmosphere. Fuel Process Technol. 2018;180:96-104.

[33] Cao X, Lu Y, Jiang J, Wang Z, Wei H, Li Y, et al. Experimental study on explosion inhibition by heptafluoropropane and its synergy with inert gas. J Loss Prev Process Ind. 2021;71.

[34] Xia Y, Zhang B, Zhang J, Wang B, Chen L, Wang R, et al. Experimental research on combined effect of obstacle and local spraying water fog on hydrogen/air premixed explosion. Int J Hydrog Energy. 2022;47:40099-115.

[35] Wen X, Wang M, Su T, Zhang S, Pan R, Ji W. Suppression effects of ultrafine water mist on hydrogen/methane mixture explosion in an obstructed chamber. Int J Hydrog Energy. 2019;44:32332-42.

[36] Nakahara K, Yoshida A, Nishioka M. Experiments and numerical simulation on the suppression of explosion of propane/air mixture by water mist. Combust Flame. 2021;223:192-201.

[37] Jing Q, Wang D, Liu Q, Chen X, Shen Y, Wang Z, et al. Inhibition effect and mechanism of ultra-fine water mist on CH4/air detonation: Quantitative research based on CFD technology. Process Saf Environ Prot. 2021;148:75-92.

[38] Zhang B, Li Z, Xia Y, Shi J, Zhang J, Wang B, et al. Experimental study on the combined effects of obstacles and local water mist on gas explosion for maritime safety. Int J Nav Archit Ocean Eng. 2022;14.

[39] Li Y, Bi M, Zhou Y, Gao W. Hydrogen cloud explosion suppression by micron-size water mist. Int J Hydrog Energy. 2022;47:23462-70.

[40] Yoshida A, Okawa T, Ebina W, Naito H. Experimental and numerical investigation of flame speed retardation by water mist. Combust Flame. 2015;162:1772-7.

[41] Cao X, Zhou Y, Wang Z, Fan L, Wang Z. Experimental research on hydrogen/air explosion inhibition by the ultrafine water mist. Int J Hydrog Energy. 2022;47:23898-908.

[42] Sugiyama Y, Shibue K, Matsuo A. The blast mitigation mechanism of a single water droplet layer and improvement of the blast mitigation effect using multilayers in a confined geometry. International Journal of Multiphase Flow. 2023;159.

[43] Wang F, Yu M, Wen X, Deng H, Pei B. Suppression of methane/air explosion in pipeline by water mist. J Loss Prev Process Ind. 2017;49:791-6.

[44] Song Y, Zhang Q. Quantitative research on gas explosion inhibition by water mist. J Hazard Mater. 2019;363:16-25.

[45] Karanam A, Sharma PK, Ganju S. Numerical simulation and validation of flame acceleration and DDT in hydrogen air mixtures. Int J Hydrog Energy. 2018;43:17492-504.

[46] Klebanoff LE, Pratt JW, LaFleur CB. Comparison of the safety-related physical and combustion properties of liquid hydrogen and liquid natural gas in the context of the SF-BREEZE high-speed fuel-cell ferry. Int J Hydrog Energy. 2017;42:757-74.

[47] Zhang B, Li Y, Liu H. Analysis of the ignition induced by shock wave focusing equipped with conical and hemispherical reflectors. Combust Flame. 2022;236.

[48] Yang Z, Cheng J, Zhang B. Deflagration and detonation induced by shock wave focusing at different Mach numbers. Chinese Journal of Aeronautics. 2023.

[49] Yu M-G, An A, You H. Experimental study on inhibiting the gas explosion by water spray in tube. Journal of China Coal Society. 2011;36.

[50] Yakovenko IS, Kiverin AD. Intensification mechanisms of the lean hydrogen-air combustion via addition of suspended micro-droplets of water. Int J Hydrog Energy. 2021;46:1259-72.

[51] Xiao H, Oran ES. Flame acceleration and deflagration-to-detonation transition in hydrogen-air mixture in a channel with an array of obstacles of different shapes. Combust Flame. 2020;220:378-93.

[52] Watanabe H, Matsuo A, Chinnayya A, Matsuoka K, Kawasaki A, Kasahara J. Numerical analysis on behavior of dilute water droplets in detonation. Proc Combust Inst. 2021;38:3709-16.

[53] Song Y, Zhang Q. Effects of Water Mist Concentration and Droplet Size on Gas-Liquid Two-Phase Detonation. Combust Sci Technol. 2023:1-18.

[54] Schunck T, Bastide M, Eckenfels D, Legendre JF. Blast mitigation by water mist: the effect of the detonation configuration. Shock Waves. 2020;30:629-44.

[55] Zhang B, Li Z, Xia Y, Shi J, Zhang J, Wang B, et al. Experimental study on the combined effects of obstacles and local water mist on gas explosion for maritime safety. Int J Nav Archit Ocean Eng. 2021.

[56] Bouvet N, Halter F, Chauveau C, Yoon Y. On the effective Lewis number formulations for lean hydrogen/hydrocarbon/air mixtures. Int J Hydrog Energy. 2013;38:5949-60.

[57] Dinkelacker F, Manickam B, Muppala SPR. Modelling and simulation of lean premixed turbulent methane/hydrogen/air flames with an effective Lewis number approach. Combust Flame. 2011;158:1742-9.

[58] Song Y, Zhang Q. Quantitative research on gas explosion inhibition by water mist. J Hazard Mater. 2019;363:16-25.

[59] Zhang P, Zhou Y, Cao X, Gao X, Bi M. Mitigation of methane/air explosion in a closed vessel by ultrafine water fog. Saf Sci. 2014;62:1-7.

[60] Cao X, Ren J, Bi M, Zhou Y, Li Y. Experimental research on the characteristics of methane/air explosion affected by ultrafine water mist. J Hazard Mater. 2017;324:489-97.

[61] Dembele S, Wen JX. Analysis of the screening of hydrogen flares and flames thermal radiation with water sprays. Int J Hydrog Energy. 2014;39:6146-59.

[62] Thomas GO. On the Conditions Required for Explosion Mitigation by Water Sprays. Process Saf Environ Prot. 2000;78:339-54.

[63] García AGM. Water droplet deformation and breakup in the vicinity of the leading edge of an incoming airfoil. 2016.

[64] Zakharov VV, Brodskaya EN, Laaksonen A. Surface tension of water droplets: A molecular dynamics study of model and size dependencies. The Journal of Chemical Physics. 1997;107:10675-83.

Figures
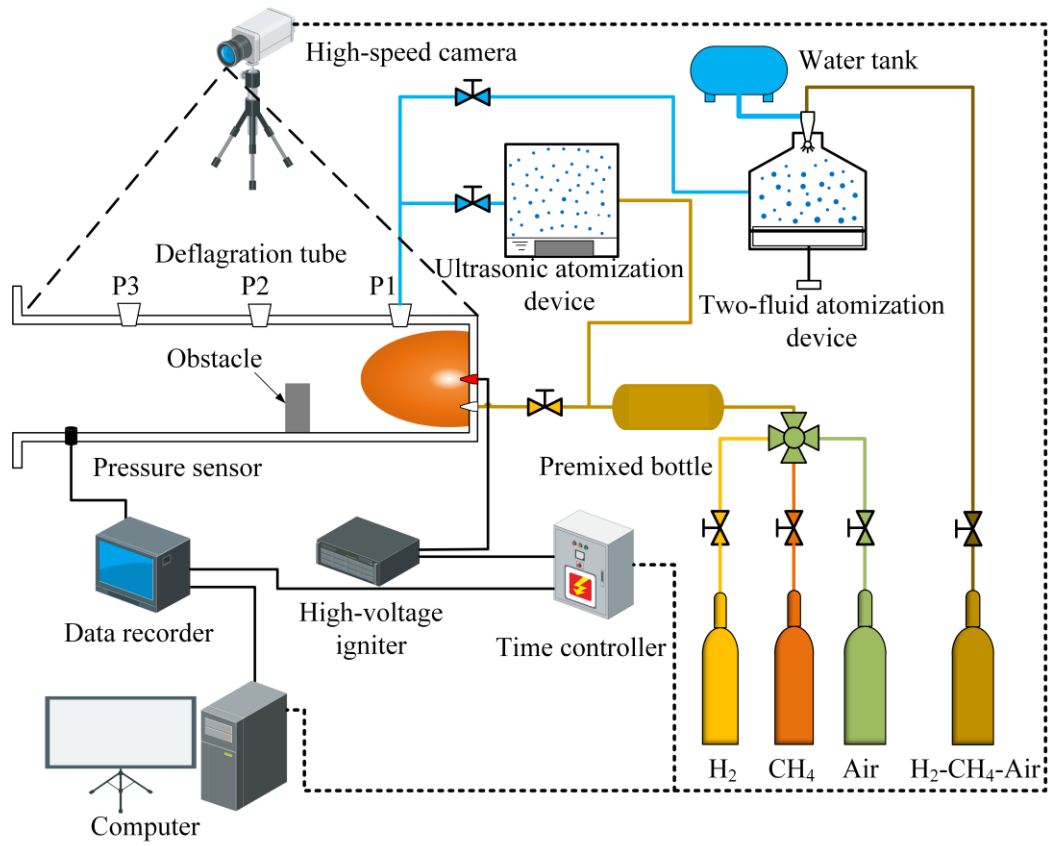
Fig. 1 Experimental system diagram.

| 8μm WM | 15μm WM | 8μm WM | 15μm WM |
| 30μm WM | 45μm WM | 30μm WM | 45μm WM |
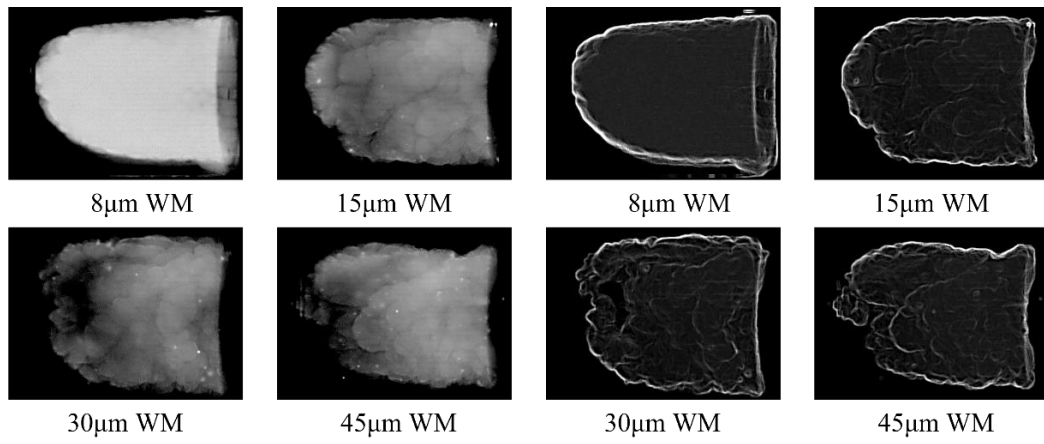
(a) Original image taken by a high-speed camera   (b) The original image processed by edge glow

Fig. 2 Flame surface morphology after using of different average size micron-level WM under ER=1.0 and HBR=10% condition without obstacle.
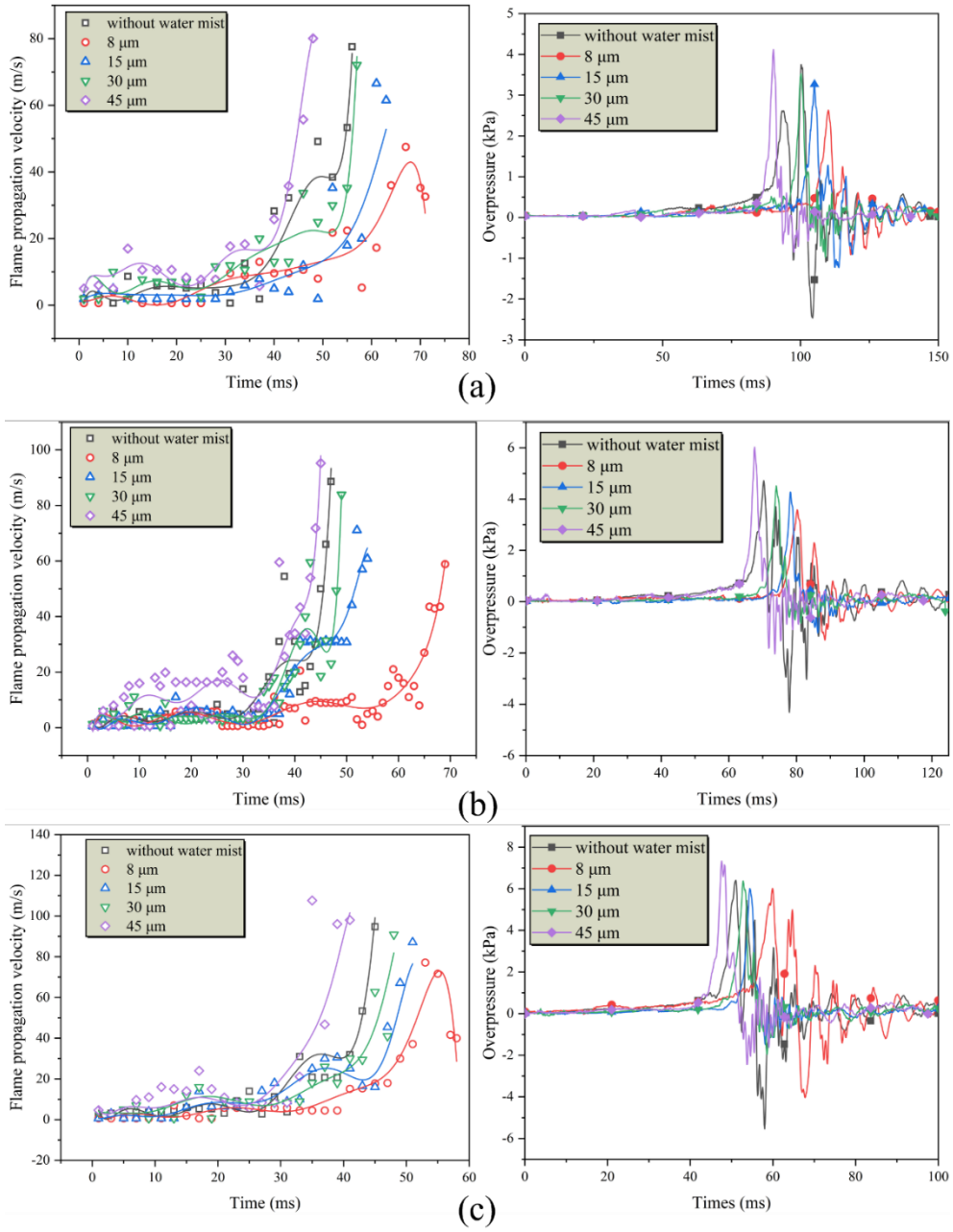
Fig. 3 Deflagration characteristic curve under the condition of micron-level WM with different average size (Φ = 1.0), (a) X = 10%; (b) X = 20%; (c) X = 30%.
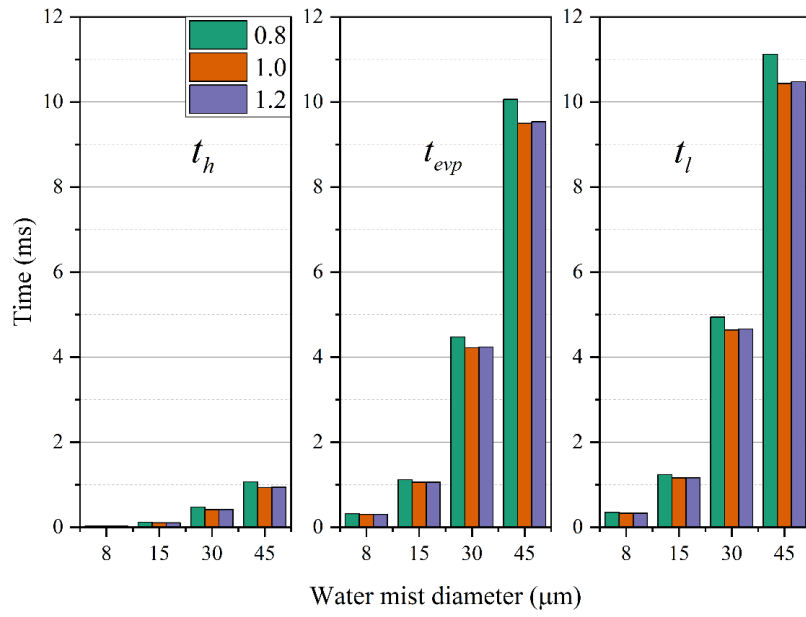
Fig. 4 Heating time, evaporation time, and lifetime of WM particles with different ER.
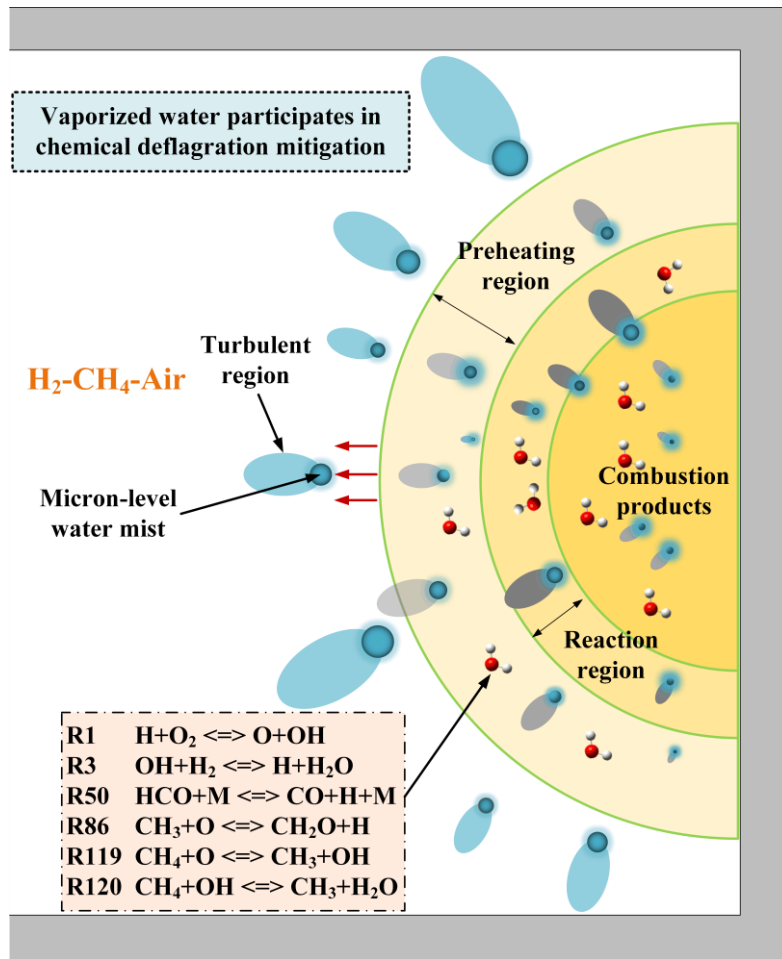
Fig. 5 Micron-level WM of different average sizes participate in the deflagration process.
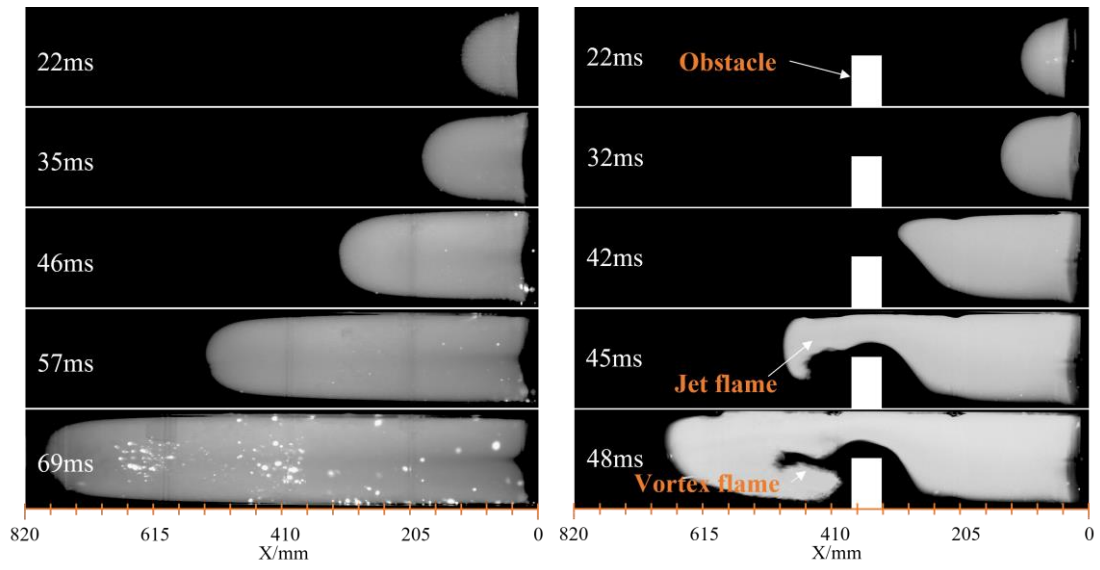
Fig. 6 Flame surface morphology with the condition of ER=1.0 and HBR=10%.
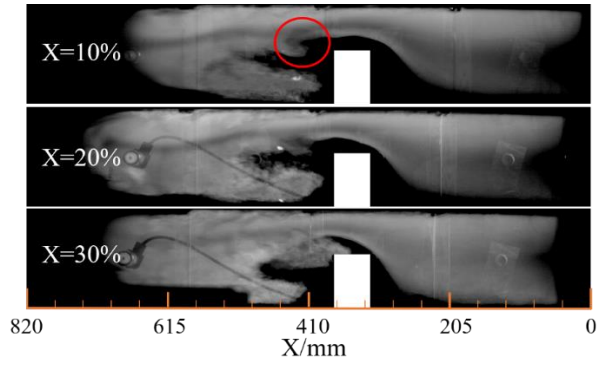
(a)
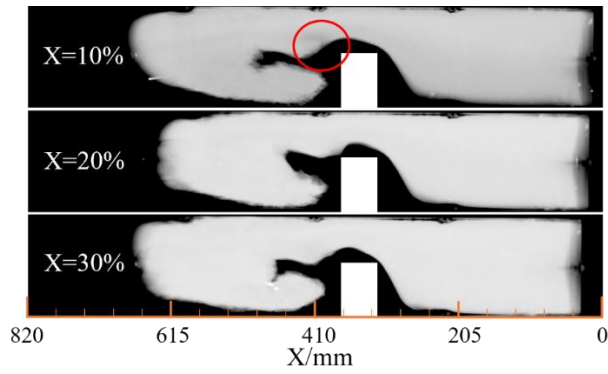
(b)
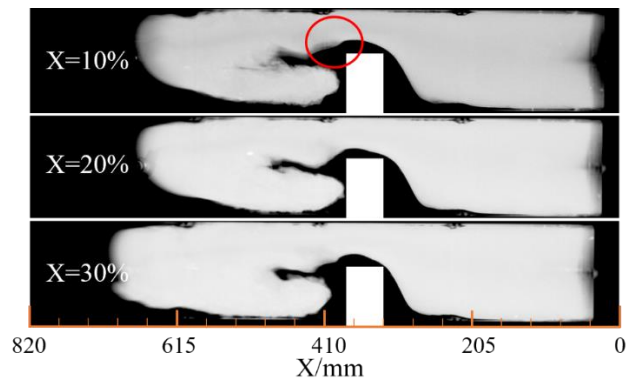
(c)

Fig. 7 Flame surface morphology under the condition of the obstacle, (a) $\Phi = 0.8$; (b) $\Phi = 1.0$; (c) $\Phi = 1.2$.

30
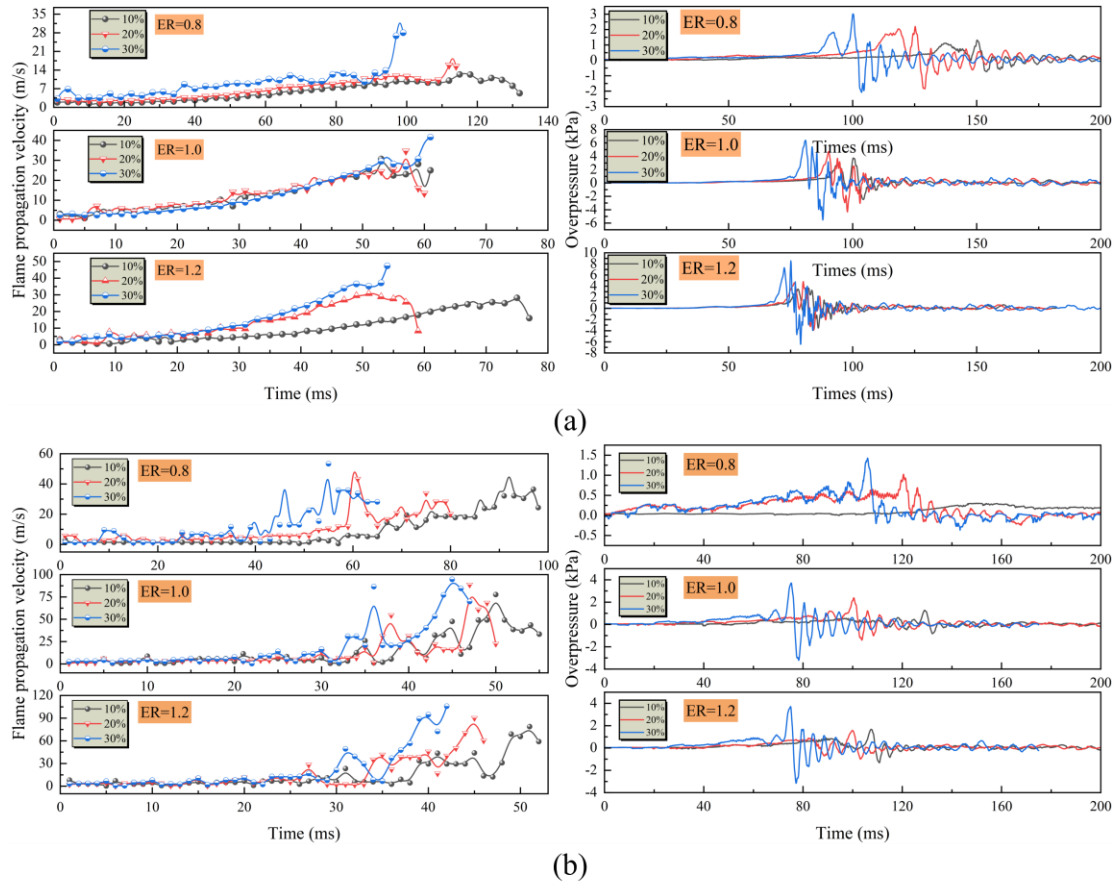
Fig. 8 Flame propagation velocity and deflagration overpressure curve; (a) Without obstacle conditions; (b) With obstacle conditions.
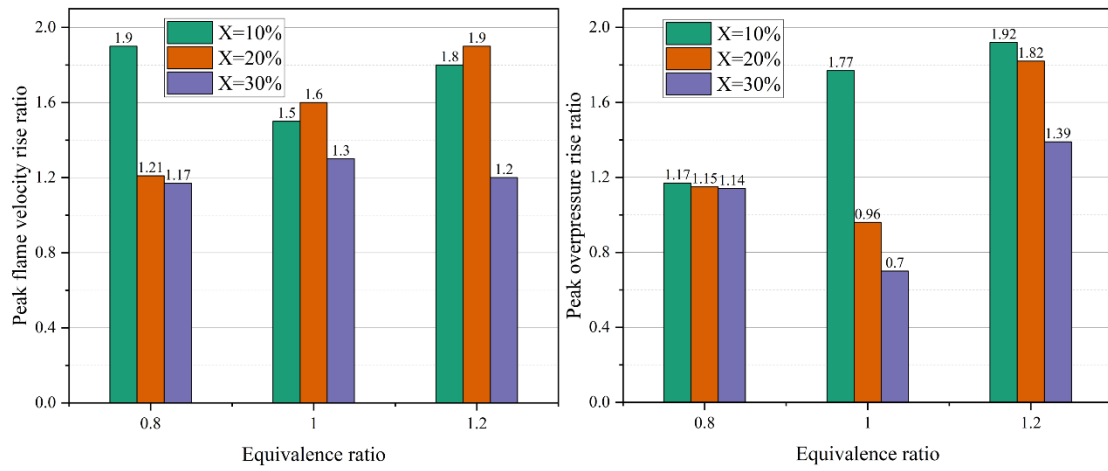
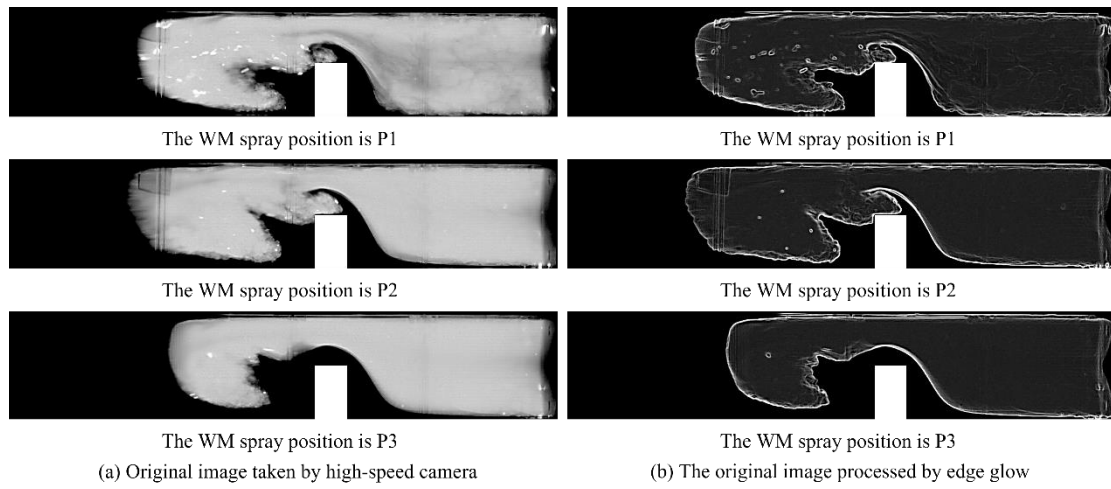Fig. 9 Peak overpressure and peak flame velocity rise ratio caused by obstacle.

The WM spray position is P1   The WM spray position is P1

The WM spray position is P2   The WM spray position is P2

The WM spray position is P3   The WM spray position is P3

(a) Original image taken by high-speed camera   (b) The original image processed by edge glow

Fig. 10 Effect of WM spray position on flame surface structure under obstacle condition.
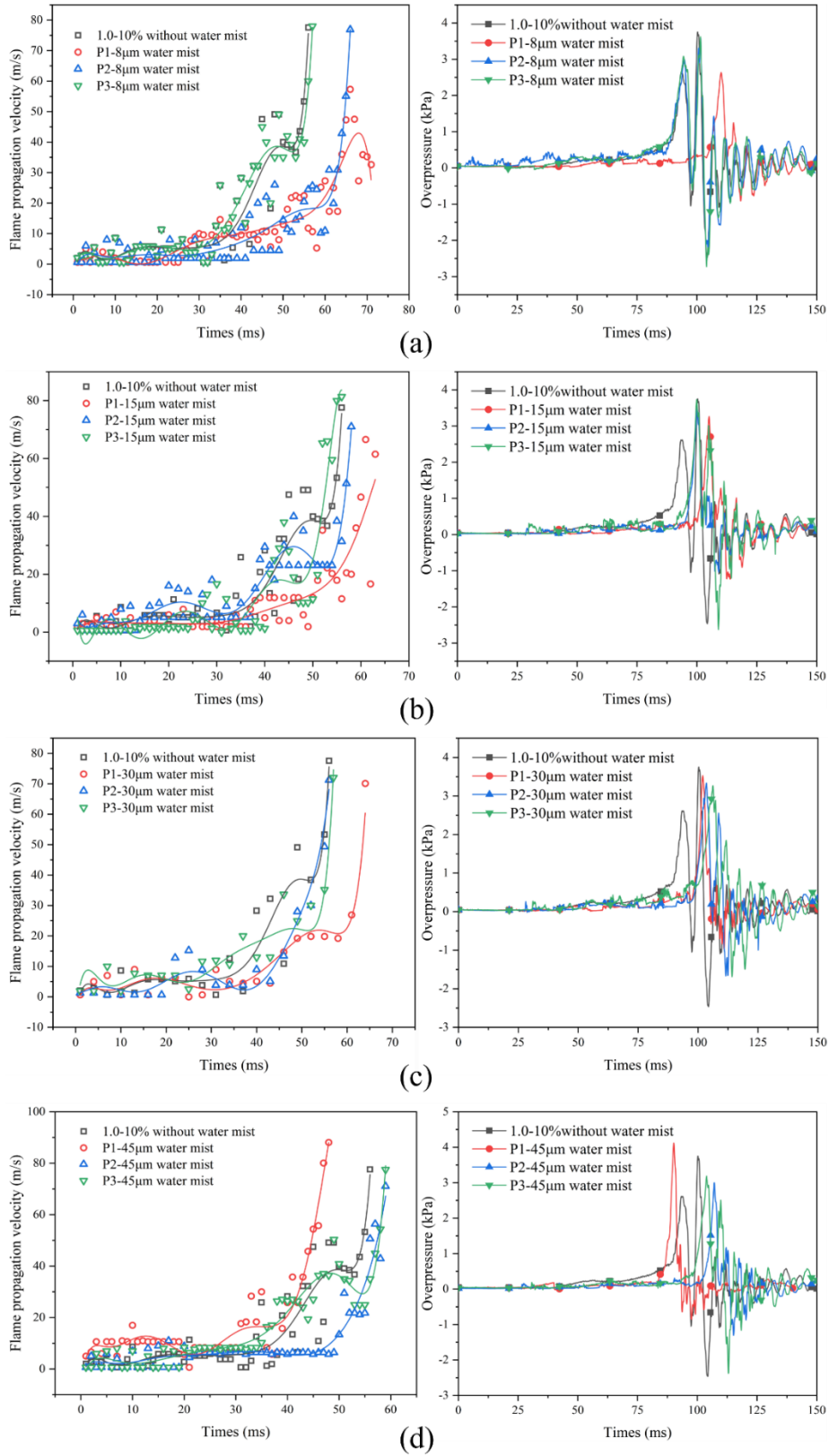
Fig. 11 Flame propagation velocity curve and deflagration pressure curve of three water mist released positions (Φ=1.0, X=10%), (a) 8 μm micron-level WM; (b) 15 μm micron-level WM; (c) 30 μm micron-level WM; (d) 45 μm micron-level WM.
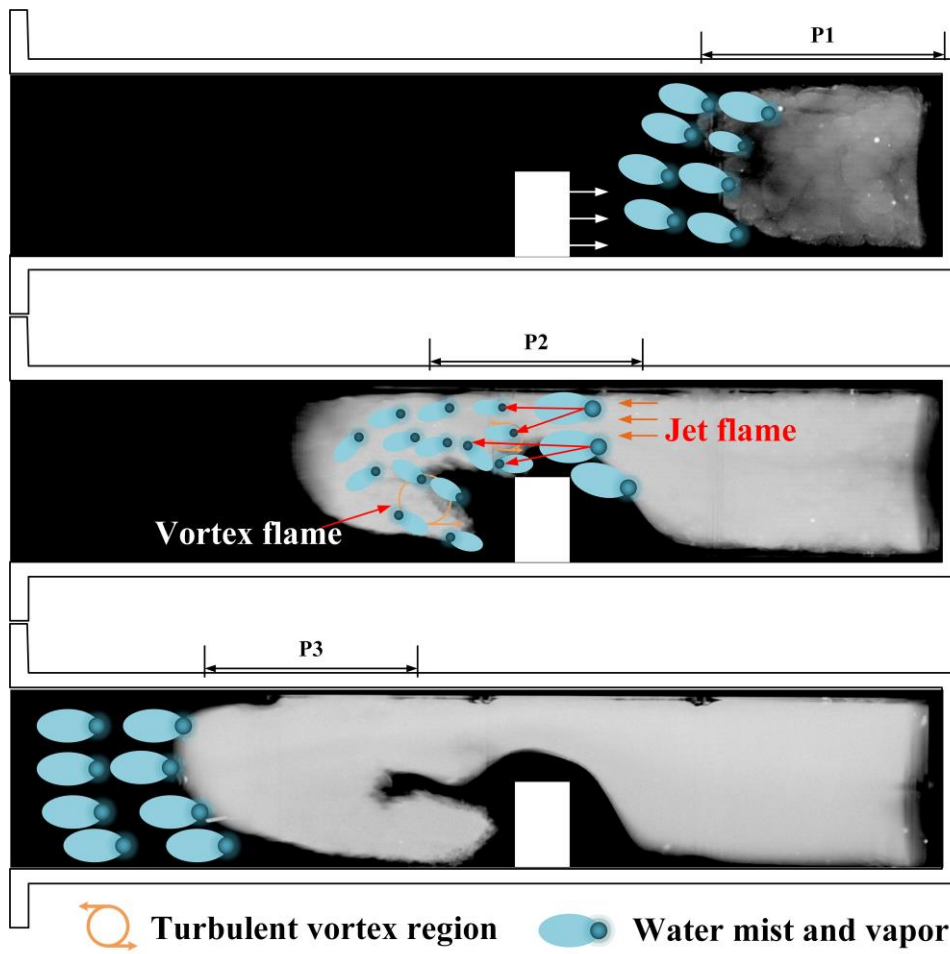
Fig. 12 Schematic diagram of the mitigation impact of WM at different local position.

Tables

Table 1 Atomization key parameters.

$\overline{d}_{32}$ (μm)	Atomization mode	Compressed gas pressure (MPa)	Hydraulic pressure (MPa)	Atomization rate (g/min)	WM spray time (s)	WM concentration (g/m³)
8	Ultrasonic atomization	/	/	2	90	586
15	Pressure type two-fluid nozzle	0.45	0.1	49.2	5	586
30	Pressure type two-fluid nozzle	0.3	0.1	49.2	5	586
45	Pressure type two-fluid nozzle	0.25	0.1	49.2	5	586

Table 2 Elementary reaction corresponding to reaction steps.

Reaction step	Elementary reaction	Reaction step	Elementary reaction
R1	$H+O_2 <=> O+OH$	R85	$CH_3+H+M <=> CH_4+M$
R3	$OH+H_2 <=> H+H_2O$	R86	$CH_3+O <=> CH_2O+H$
R14	$H+O_2+H_2O <=> HO_2+H_2O$	R93	$CH_3+HO_2 <=> CH_3O+OH$
R15	$H+O_2+N_2 <=> HO_2+N_2$	R101	$2CH_3+M <=> C_2H_6+M$
R21	$HO_2+O <=> OH+O_2$	R118	$CH_4+H <=> CH_3+H_2$
R22	$HO_2+OH <=> O_2+H_2O$	R119	$CH_4+O <=> CH_3+OH$
R23	$2HO_2 <=> O_2+H_2O_2$	R120	$CH_4+OH <=> CH_3+H_2O$
R50	$HCO+M <=> CO+H+M$		

Nomenclature

Nomenclature	
$\overline{d}_{32}$	Sauter mean diameter of micron-level water mist, (μm)
n	Micron-level water mist particles number
d	Micron-level water mist particles diameter, (μm)
ω	Local concentration of micron-level water mist, (g/m^3)
W_f	Flux of micron-level water mist, (g/s)
V	The volume of the local micron-level water mist released region, (m^3)
Φ	Equivalence ratio
$n_{hydrogen}$	Moles of hydrogen, (mol)
n_{air}	Moles of air, (mol)
X_{H_2}	Hydrogen blending ratio
V_{H_2}	Volume of hydrogen, (m^3)
V_{CH_4}	Volume of methane, (m^3)
t_l	Micron-level water mist particles lifetime, (ms)
t_h	The time required for micron-level water mist particles to rise from room temperature to 100 °C, (ms)
t_{evp}	The time it takes for micron-level water mist particles to vaporize from liquid at 100 °C to gas at 100 °C, (ms)
R_v	Peak flame velocity rise ratio
R_P	Peak overpressure rise ratio
$v_{obstacle}$	Peak flame velocity under obstacle condition, (m/s)
v	Peak flame velocity under no obstacle condition, (m/s)
$P_{obstacle}$	Peak overpressure under obstacle condition, (kPa)
P	Peak overpressure under no obstacle condition, (kPa)
W_e	Weber number, (dimensionless)
ρ_g	Gas density, (kg/m^3)
u_g	Gas flow velocity, (m/s)
σ	Surface tension of water, (N/m)
Abbreviations	
LWM	Localized water mist
ER	Equivalence ratio
HBR	Hydrogen blending ratio
PFPV	Peak flame propagation velocity
PDOP	Peak deflagration overpressure